Journal of Materials Chemistry A

ROYAL SOCIETY OF CHEMISTRY

PAPER

View Article Online
View Journal | View Issue

Cite this: J. Mater. Chem. A, 2026, 14, 20996

Heating-rate controlled defect engineering in $BiVO_4$ thin films for enhanced photoelectrochemical water splitting

Rafiqat Ul Rasool, [a] Syed Bilal Ahmed [b] and Ruiqin Zhang *[ac]

We investigate the effect of nucleation kinetics, governed by ramping rate of annealing temperature, on the structural, chemical, and optical properties of $BiVO_4$ thin films and their subsequent impact on photoelectrochemical (PEC) performance, with the goal of enhancing the photocatalytic activity of $BiVO_4$-based photoanodes. Here, we demonstrate that controlled thermal nucleation, achieved by tuning the annealing heating rate, is an effective and scalable strategy to engineer oxygen vacancies (O_v) and modulate defect chemistry in $BiVO_4$ thin films. Structural and spectroscopic analyses reveal that an optimized heating rate promotes the partial reduction of V^{5+} to V^{4+}, generating O_v donor states that narrow the optical band gap from 2.55 to 2.33 eV and increase carrier density. First-principles DFT calculations demonstrate that these oxygen vacancies introduce V^{4+} derived shallow donor states, providing theoretical validation for the experimentally observed bandgap reduction and enhanced charge transport. Atomic force microscopy (AFM) and scanning electron morphology (SEM) reveals an evolution in surface morphology with increased surface roughness and porosity, which promote electron transport and bulk conductivity. These synergistic effects result in a remarkable photocurrent density of 3.17 mA cm^{-2} at 1.23 V *vs.* the reversible hydrogen electrode (RHE) and excellent stability for ~4.5 hours in aqueous electrolyte. Overall, this study highlights controlled thermal nucleation as a robust strategy to tune microstructure, defect chemistry, and charge transport, paving the way for next-generation high-efficiency PEC materials.

Received 1st May 2025
Accepted 8th April 2026

DOI: 10.1039/d5ta03464g

rsc.li/materials-a

1 Introduction

Photoelectrochemical (PEC) cells, which utilize photoactive semiconductors and sunlight to produce electricity and hydrogen through water splitting, represent a promising alternative to natural photosystems.[1–4] This process stores solar energy in the H–H bond, the simplest chemical bond,[5,6] and was first demonstrated using nanosized titania (TiO_2).[7] Various semiconductors have been developed for water electrolysis,[8–10] including III-V semiconductors (*e.g.*, $GaInP_2$,[11] AlGaAs,[12] and InP[13]) and II-VI semiconductors (*e.g.*, ZnO,[14] CdS,[15] and ZnS[16]), which exhibit good photoactivity with solar-to-hydrogen (STH) conversion efficiencies of up to 20%. However, these materials face limitations due to their instability in aqueous electrolytes and high costs.[17–19] In contrast, metal oxides are more durable and cost-effective, but their reported STH conversion efficiencies are typically below 8%,[20–22] limited by rapid charge carrier recombination and poor charge transport.[10,23]

Monoclinic scheelite $BiVO_4$ has emerged as a promising metal oxide photoelectrode due to its favorable band structure (E_g ~2.3–2.6 eV), suitable band-edge position (conduction band at ~0 V *vs.* RHE), and intrinsic electrical properties.[24–26] It is one of the three polymorphs of $BiVO_4$, *i.e.* pucherite (orthorhombic), dreyerite (tetragonal zircon), and clinobisvanite (monoclinic scheelite).[27] Its crystallographic and electronic properties show good photocatalytic activity.[28,29] However, $BiVO_4$ suffers from significant charge carrier recombination under illumination due to its low charge carrier mobility (~0.043 $cm^2\ V^{-1}\ s^{-1}$).[30] The highest reported photocurrent density for pristine $BiVO_4$ is around 3.6 mA cm^{-2},[31] achieved using laser ablation methods that are not scalable due to decreasing ablation efficiency over time, high energy requirements, and expensive production systems. Therefore, developing facile protocols to enhance the charge carrier transport in $BiVO_4$ photoanodes remains a significant challenge. Various approaches have been explored, including doping,[32,33] heterojunction formation,[34,35] plasmonics,[36,37] and nanostructuring.[38] Additionally, optimizing experimental parameters such as precursor concentration,[39,40] ultrasonication treatment,[41,42] thermal treatment,[43,44] and annealing conditions[45,46] has been shown to significantly

[a]Department of Physics, City University of Hong Kong, Hong Kong 999077, China. E-mail: aprqz@cityu.edu.hk

[b]Division of Science, Engineering, and Health Studies (SEHS), School of Professional Education & Executive Development, The Hong Kong Polytechnic University, Hong Kong SAR, China

[c]Advanced Energy Storage Technology Research Center, Shenzhen Polytechnic University, Shenzhen 518055, China

impact the morphology and performance of these materials for photo-driven applications.

This work demonstrates that the heating rate during annealing is an effective parameter for controlling nucleation that governs defect formation, and the resulting microstructure in $BiVO_4$. By tuning oxygen vacancy concentration through this simple thermal adjustment, we provide a scalable and industry-compatible approach for improving charge transport and PEC performance. Oxygen vacancies introduce distinct electronic states by redistributing charges in $BiVO_4$, reducing the work function and bandgap, thereby enabling the thin films to absorb lower-energy light.[47–49] Optimizing the thermal treatment during the deposition of $BiVO_4$ thin films is a crucial approach to tuning the nucleation process, which defines the crystallographic properties of the final product.[50] This thermal treatment is decisive in tailoring the crystal structure and generating oxygen vacancies that enable effective charge migration from the bulk material to the surface, thereby enhancing light absorption efficiency.[47,50] Practically, the effective activation energy for nucleation and crystallization can be tuned by varying the heating rate during the annealing process.[51,52] The impact of the heating rate on the crystallization of $BiVO_4$ thin films was investigated using X-ray diffraction (XRD) and atomic force microscopy (AFM). The results show that the crystallinity and grain size of the films are strongly influenced by the heating rate.[53,54] Optimizing the annealing protocol through a series of experiments resulted in a remarkable five-fold increase in photocurrent density, reaching 3.17 mA cm^{-2} at 1.23 V *vs.* RHE. X-ray photoelectron spectroscopy (XPS), UV-visible spectroscopy, and AFM analyses confirmed that tuning the annealing parameters altered the interatomic bonding, lowered the work function, and refined the film morphology to enhance the photoactivity of $BiVO_4$, providing a facile and effective alternative to address the limitations of charge generation and transport in $BiVO_4$ photoelectrodes.

2 Experimental details

2.1. Materials

All chemicals were purchased from Sigma Aldrich and used in their purest form without further treatment. The $BiVO_4$ ink was prepared using $Bi(NO_3)_3 \cdot 5H_2O$ (≥99.99%), ethylene glycol (≥99.0%), glacial acetic acid (≥99.7%)) deionized water, $VO(acac)_2$ (≥98%), and polyethylene glycol (≥99.0%). The electrolyte solution consisted of deionized water, Na_2SO_4 (≥99.0%), and Na_2SO_3 (≥98%).

2.2. Preparation of $BiVO_4$ ink

The synthesis of $BiVO_4$ thin films was performed in air. 0.6 g of $Bi(NO_3)_3 \cdot 5H_2O$ was added to 4.0 g (3.604 mL) of ethylene glycol (EG) and sonicated for 10 minutes to achieve transparency. Subsequently, 2.0 mL of glacial acetic acid and 1.0 mL of deionized water were added and sonicated for an additional 10 minutes. Adding 0.6 g of $VO(acac)_2$ and sonicating for 30 minutes transformed the transparent solution into a dark turquoise color. Finally, 0.472 g of polyethylene glycol (PEG) was added to control the morphology of the deposited $BiVO_4$ thin films. The resulting viscous solution, stabilized by the triblock copolymer Pluronic F-108, was ready for spin coating.

2.3. Fabrication of $BiVO_4$ film

FTO-coated glass substrates were cleaned ultrasonically in acetone, ethanol, and deionized water for 20 minutes each, followed by drying at 60 °C. The $BiVO_4$ films were deposited by spin coating 0.5 mL of the $BiVO_4$ ink onto the FTO-coated glass substrates at 1200 rpm for 10 seconds and then 1500 rpm for 35 seconds. The films were immediately transferred to a furnace for annealing at 475 °C for 1.5 hours with different heating rates (10 °C, 20 °C, 30 °C, 40 °C, 50 °C, 60 °C, and 70 °C per minute), labeled as BV-10 °C, BV-20 °C, BV-30 °C, BV-40 °C, BV-50 °C, BV-60 °C, and BV-70 °C, respectively. The samples were allowed to cool naturally to room temperature. The entire process took approximately 12 hours, producing films with a thickness of 0.2 microns. A single spin-coating step was sufficient to prepare all seven samples with different heating rates. The experimental protocol is illustrated in Fig. 1, and digital micrographs of the prepared samples are provided in the SI (Fig. S1).

2.4. Characterization techniques

X-ray powder diffraction (XRD; Bruker D8 ADVANCE Plus) was performed to obtain the crystal structures of the prepared samples using Cu-Kα radiation (wavelength 1.5 Å) over a range of 10°–80° at a scan rate of 5° min^{-1}. X-ray photoelectron spectroscopy (XPS; ThermoFisher ESCALAB™ 250XIb) equipped with Al Kα radiation was conducted to explore the binding energy of all elements. UV-vis spectroscopy (Cary 50 conc UV-visible spectrophotometer) was performed in the range of 300–700 nm. AFM (Bruker diMultimode V®AFM) data were obtained using Nanoscope software and an AppNano ACTA tip (ROC = 6 nm) in tapping mode.

2.5. PEC cell assembly and measurements

The PEC performance of the $BiVO_4$ thin films was tested using a standard three-electrode cell system in a deionized water-based electrolyte (0.1 M Na_2SO_4 + 0.1 M Na_2SO_3; pH ~9.26). The prepared $BiVO_4$ thin films were cut into smaller pieces with an effective area of 0.7 cm^2, and the edges were sealed with epoxy glue to prevent current leakage. Before use, the electrolyte was purged with nitrogen gas for 30 minutes to remove any residual dissolved oxygen. The $BiVO_4$ photoanode served as the working electrode, while a platinum wire and an Ag/AgCl electrode were used as the counter and reference electrodes, respectively. The applied potential was corrected using the Nernst equation:

$$E_{RHE} = E_{SCE} + 0.0591\ pH + 0.209 \quad (1)$$

where E_{RHE} is the reversible hydrogen electrode potential, and 0.209 is the conversion factor from Ag/AgCl to RHE. All PEC data were recorded using a CH Instrument electrochemical workstation (model CHI6011E). A 300W Xenon lamp (NewBet HSX-F300) provided simulated 1 sun (AM 1.5 G) illumination with

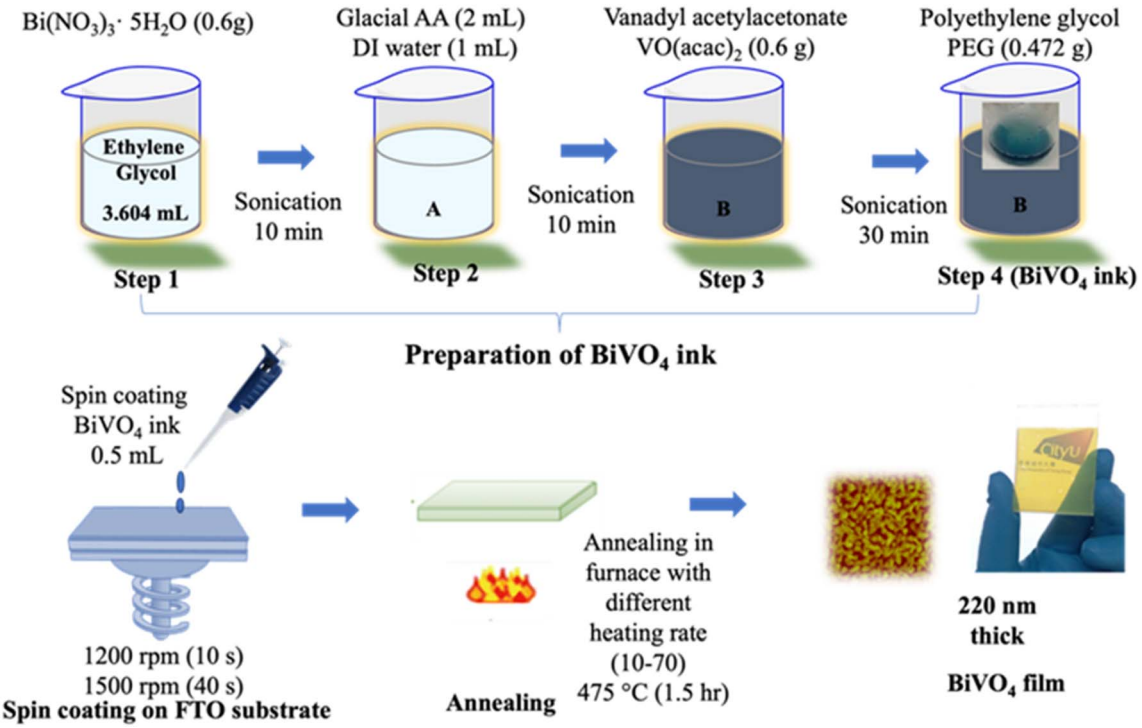

Fig. 1 The schematic illustration of $BiVO_4$ thin films deposition protocol by spin coating method.

a calibrated power density of 100 mW cm^{-2}. Transient photocurrent density was measured under chopped illumination at 1.23 V *vs.* RHE.[53] Linear sweep voltammetry (LSV) was conducted at a scan rate of 10 mV s^{-1}, and electrochemical impedance spectroscopy (EIS) was performed in the frequency range of 1 Hz to 10 kHz. The flat-band potential was estimated from Mott–Schottky (MS) plots using the capacitance data of the $BiVO_4$ photoanodes recorded at different biases. A sinusoidal modulation of 5 mV at 5 Hz was applied to obtain the MS plots:

$$\frac{1}{C^2} = \frac{2\left(V - V_f - \frac{kT}{e}\right)}{e\varepsilon\varepsilon^{\circ}N_d\ A^2} \quad (2)$$

where C is the capacitance of photoanode, e is the electronic charge (C), ε is the dielectric constant of $BiVO_4$, ε^{o} is the permittivity of free space, V is the applied bias (*versus* RHE), V_f is the flat band potential (*versus* RHE), k is the Boltzmann constant, N_d is the donor density for n-type semiconductor (cm^{-3}), A is the surface area of photoanode, and T is the temperature (K).

2.6. Computational methods

All density functional theory (DFT) calculations were performed using the Vienna *Ab initio* Simulation Package (VASP).[55,56] The electron–ion interactions were described using the Projector Augmented-Wave (PAW) method with the Perdew–Burke–Ernzerhof (PBE) exchange-correlation functional.[57,58] To accurately model the electronic structure of $BiVO_4$, the DFT + U method was employed with a Hubbard U parameter of 3.0 eV applied to the Bi 3d states. The pristine monoclinic structure was first fully relaxed to its minimum energy configuration. A 2 × 1 × 2 supercell containing 96 atoms was then constructed from this optimized cell to model bulk properties. A neutral oxygen vacancy was created by removing a single oxygen atom, after which the defective supercell was also fully relaxed. The Brillouin zone for all supercell calculations was sampled with a Γ-centered 2 × 3 × 2 k-point mesh.[59]

3 Results and discussion

3.1. Crystallographic analysis

Fig. 2 shows the XRD patterns of $BiVO_4$ thin films prepared under different heating rates. The obtained diffraction peaks are in good correspondence with the monoclinic scheelite phase of $BiVO_4$ (JCPDS card number 14-0688), which is optimal for photoelectrochemical water splitting applications.[53] Some additional peaks were attributed to the FTO substrates, and no secondary oxide phases were detected in any of the films.

All films subjected to various thermal treatments exhibited comparable patterns, indicating no phase transformation. Further analysis revealed that BV-60 °C exhibited the highest crystallinity, with sharper diffraction peaks compared to other samples. The sharpness of the peaks is directly proportional to the crystallite size.[60] The controlled annealing process played an important role in tuning the crystallinity and consequently the electronic properties of the $BiVO_4$ thin films. Higher crystallinity reflects improved charge transport, which is essential for enhancing the performance of photoactive materials.[61,62] The magnified plotting of XRD peaks for better comparison is provided in the SI (Fig. S2), and the planes associated with each peak are listed in SI Table S3.

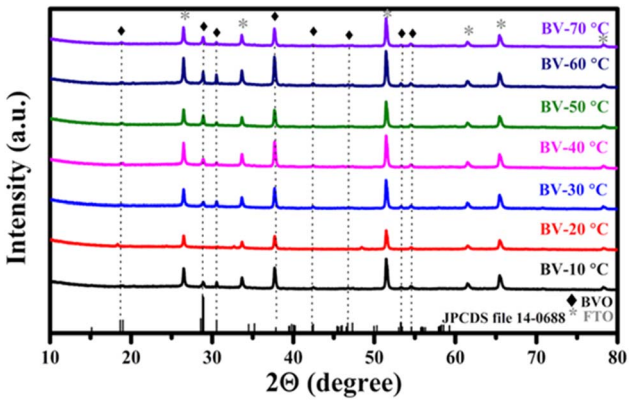

Fig. 2 XRD patterns of $BiVO_4$ thin films annealed at different heating rates (BV-10 °C to BV-70 °C). All samples match the monoclinic scheelite phase (JCPDS 14-0688), with increasing peak sharpness and intensity at higher heating rates, indicative of improved crystallinity. The peaks from the FTO substrate are marked with (*).

3.2. X-ray photoelectron spectroscopy (XPS)

The surface chemical status of the samples was studied using XPS. Fig. 3a shows the survey spectra of $BiVO_4$, confirming the presence of C, Bi, V, and O elements in all samples. The Bi $4f_{7/2}$ and Bi $4f_{5/2}$ peaks (Fig. 3b) for BV-20 °C, BV-40 °C, BV-50 °C, and BV-70 °C were observed at 159.4 eV and 164.7 eV, respectively, indicating the Bi^{3+} oxidation state. The peak shift is negligible among these samples, except for BV-10 °C and BV-30 °C, which exhibited a slight negative shift towards lower binding energies. The sample BV-60 °C showed the lowest binding energies (158.9 eV and 164.2 eV), suggesting a change in the local coordination environment due to the presence of oxygen vacancies and V^{4+} species.

The V $2p_{3/2}$ and V $2p_{1/2}$ peaks observed at 516.8 eV and 524.6 eV (Fig. 3d) are characteristic of V^{5+} species.[63–67] BV-60 °C exhibited a prominent low-energy shift in both the Bi 4f and V 2p binding energies compared to other samples. This shift can be attributed to changes in the local coordination environments of Bi and V ions, specifically a reduction in coordination number due to oxygen vacancies, which likely leads to the partial reduction of Bi^{3+} and V^{5+} ions.[67]

XPS analysis of metal oxides revealed two types of oxygen oxidation states: the peaks formed in the range of 529.5–530.5 eV are the splitting peaks of the O 1s band, characteristic of the O^{2-} oxidation state. The peaks formed in the region between 531–532 eV suggest the existence of another O 1s species with lower electron density than O^{2-}, assignable to O^{-} ions.[68,69] The major peaks for BV-10 °C, BV-30 °C, BV-40 °C, and BV-70 °C were observed at 530.07 eV and 530.90 eV in the O 1s spectrum (Fig. 3c), assigned to O bonded within a regular oxide crystal (O^{2-}) in $BiVO_4$ and adsorbed hydroxyl groups on the surface, respectively. BV-20 °C and BV-50 °C exhibited lower binding energy values without changes in oxidation states. The presence of oxygen vacancies in BV-60 °C is evident from the shoulder peak at 531.5 eV (Fig. 3c, inset), indicating the incorporation of V^{4+} species in the $BiVO_4$ lattice during the reaction between $Bi(NO_3)_3$ and $VO(acac)_2$. The partial reduction of V^{5+} to V^{4+} ions leads to the generation of abundant oxygen vacancies as shallow donors of electrons.[68,70,71] The higher concentration of V^{4+} species and oxygen vacancies in BV-60 °C can be attributed to its porous network structure, which provides a larger surface area for defect formation, thereby enhancing the photocatalytic performance of $BiVO_4$.[72] The lower binding energy shifts in other samples for Bi and V splitting signals indicate lower crystallinity compared to BV-60 °C, consistent with the XRD results.

Collectively, the systematic shifts in the Bi 4f, V 2p, and O 1s spectra across the heating-rate series establish a clear comparative trend in defect density. The defect-related O 1s shoulder at $\sim$531.0 $\pm$ 0.2 eV is observed in all samples. By normalizing each spectrum to the lattice oxygen maximum ($\sim$529.6–530.0 eV) and inspecting a fixed binding-energy window (530.8–531.6 eV), we find that the vacancy-related intensity is most pronounced for BV-60 °C, followed by BV-50 °C $\gtrsim$ BV-40 °C > BV-30 °C $\approx$ BV-70 °C > BV-20 °C $\approx$ BV-10 °C. A similar trend is evident in the V $2p_{3/2}$ spectra, where the relative contribution of the V^{4+} shoulder ($\sim$516.0–516.5 eV) compared to the V^{5+} main peak ($\sim$516.8 eV) is again maximized for BV-60 °C. This concurrent increase in vacancy-related oxygen and V^{4+} species provides consistent evidence that BV-60 °C possesses the highest oxygen-vacancy concentration. Importantly, this sample also exhibits the strongest photoelectrochemical response, including the highest photocurrent density and charge-separation efficiency, confirming the functional role of these vacancies. We emphasize that this comparison is semi-quantitative; however, by applying identical normalization and fixed energy windows across the series, the observed trend is robust and reliable.

3.3. UV-visible spectroscopy

Investigating the optical properties is crucial for understanding the PEC performance. Fig. 4(a and b) shows the UV-vis absorption spectra of the $BiVO_4$ thin films annealed at different heating rates, along with bandgap evaluations using the Tauc relation (eqn (3)):

$$\alpha h\nu = C\,(h\nu - E_g)^{n/2} \quad (3)$$

where α is the absorption coefficient, h is the Plank's constant, ν is the frequency of incident light, C is a constant which is the function of band telling parameter, and E_g is the bandgap energy (eV). For $BiVO_4$, $n = 1$ since it is an indirect bandgap semiconductor.[73] The visible light absorption in monoclinic scheelite $BiVO_4$ occurs through transitions from the valence band (composed of Bi 6s or Bi 6s + O 2p hybrid orbitals) to the V 3d conduction band.[74] All samples exhibited strong absorption in the visible light region, with the most intense absorption observed in BV-60 °C. The bandgap reduction from 2.55 eV to 2.33 eV in BV-60 °C is attributed to the introduction of shallow bands within the bandgap of $BiVO_4$ by oxygen vacancies.[75] These electronic defects significantly reduce the bandgap energy, promoting the photoactivity of the material, as illustrated in Fig. 4c.

The optical response further clarifies the role of defect states in charge dynamics. A gradual narrowing of the band gap from

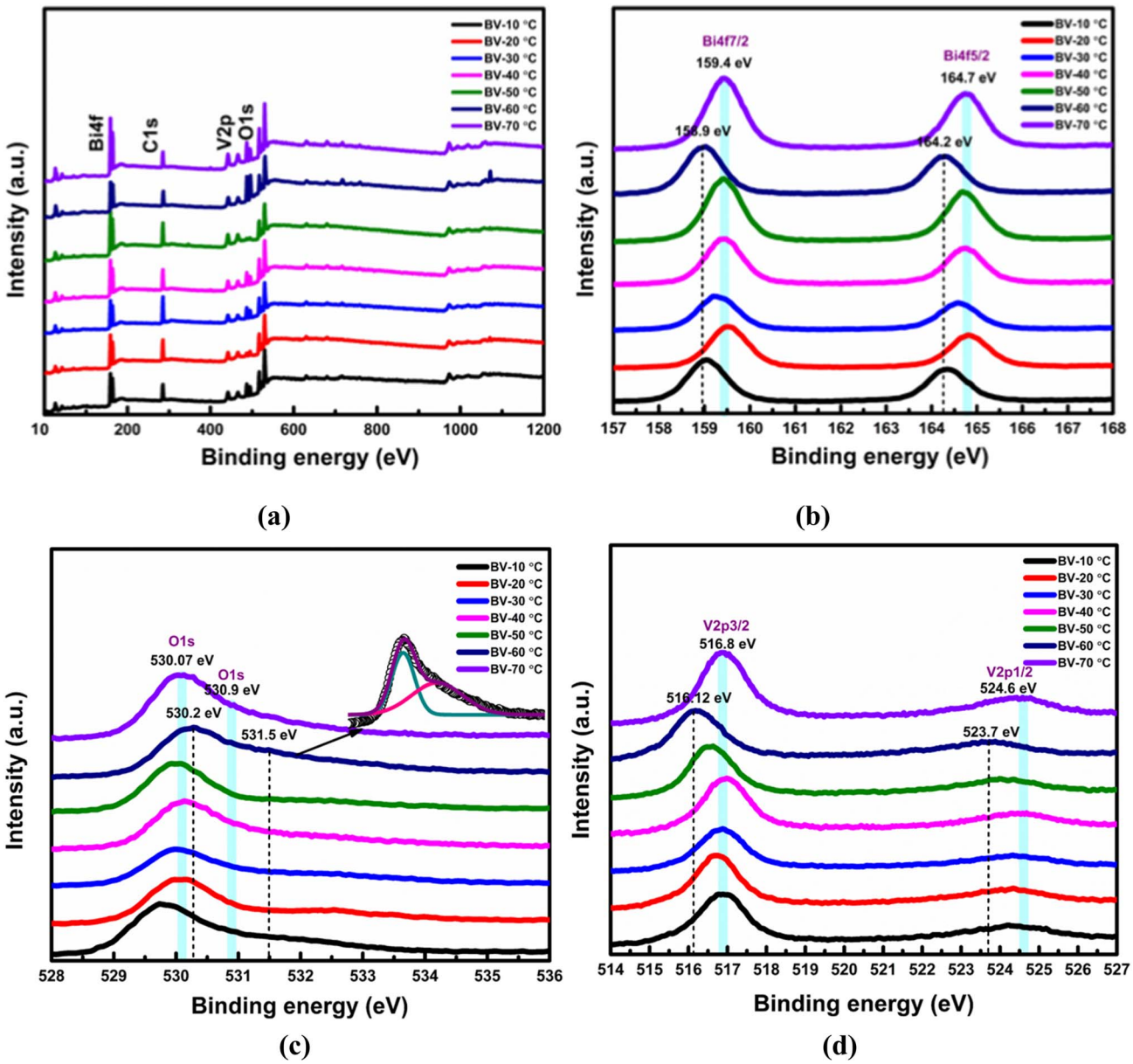

Fig. 3 (a) XPS high resolution elemental survey plots confirming the presence of Bi 4f, V 2p, and O 1s bands, (b) the splitting signals of Bi 4f to Bi $4f_{7/2}$ and Bi $4f_{5/2}$, (c) the O 1s peaks observed for as deposited $BiVO_4$ samples with an obvious peak observed at 531.5 eV for BV-60 °C referring to the presence of oxygen vacancies in this sample, and (d) the splitting signals of V 2p to V $2p_{3/2}$ and V $2p_{1/2}$.

~2.55 eV (BV-20 °C) to ~2.33 eV (BV-60 °C), together with the emergence of sub-bandgap absorption tails, can be attributed to oxygen-vacancy/V^{4+} defect states just below the conduction band. These defect states effectively extend light absorption and facilitate electron transfer. Complementary PL measurements (S4) reveal that samples with the highest PL intensity, such as BV-40 °C, suffer from pronounced radiative recombination, which limits charge carrier utilization and results in lower PEC activity. In contrast, BV-60 °C exhibits strongly quenched PL, indicating suppressed recombination and better separation of photogenerated carriers. This behaviour arises from favourable band-edge modulation by optimally introduced oxygen vacancies as the defect states below the conduction band promote electron delocalization while maintaining sufficient band bending at the electrode/electrolyte interface to drive water oxidation. The same sample (BV-60 °C) delivers the highest photocurrent density, confirming that reduced PL intensity directly correlates with improved charge separation and PEC performance. Excessive vacancy formation at higher annealing rates (BV-70 °C) partially restores PL intensity, reflecting recombination *via* deep defect centres, and explains the corresponding decline in PEC activity.

3.4. Atomic force microscopy (AFM)

AFM images (5 × 5 μm) of the $BiVO_4$ thin films reveal a morphology transition from densely stacked short nanorods

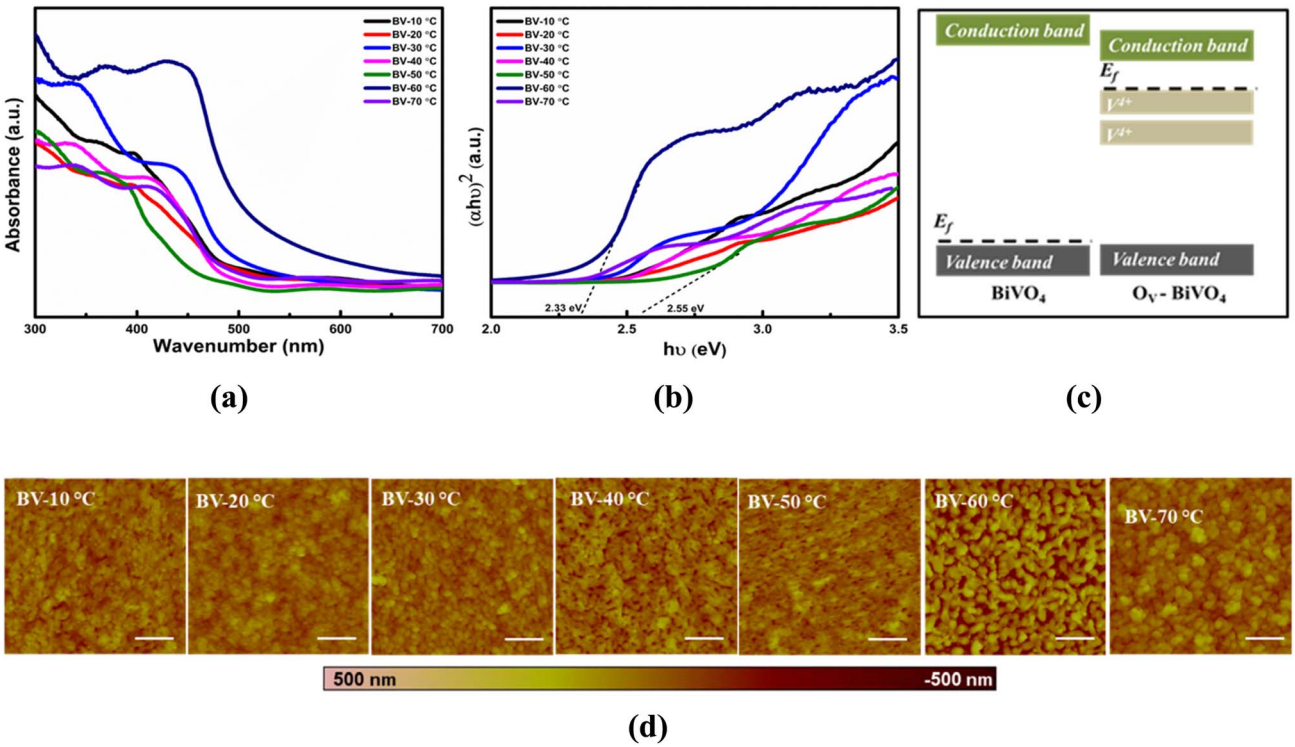

Fig. 4 (a) UV-vis absorption spectra of $BiVO_4$ thin films prepared at different heating rates, showing improved visible-light absorption for BV-60 °C. (b) Tauc plots for bandgap estimation, with the lowest E_g (~2.33 eV) observed for BV-60 °C. (c) Schematic representation of shallow donor levels introduced by oxygen vacancies, which facilitate charge transport. (d) AFM images revealing morphology evolution from compact grains (BV-10-40 °C) to well-defined nanocones at BV-60 °C, before collapsing into larger irregular features at BV-70 °C. The rougher, porous morphology of BV-60 °C provides enhanced surface area and charge-separation pathways, consistent with its improved PEC activity.

to long, sharp nanocones with a globular particle matrix for BV-60 °C. The average arithmetic roughness (R_a), root mean square roughness (R_q), and average maximum height (R_{mp}) were estimated from AFM analysis and are summarized in Table 1. The three-dimensional topographic images of the as-deposited $BiVO_4$ thin films are shown in Fig. 4d. BV-60 °C exhibited the highest roughness values and the most pronounced nanocones. Compared to other samples (Table 1), the vertically oriented nanocone array provides a greater contact area between the electrolyte and the photoanode, as well as a larger particle size. Since conductivity is directly proportional to the cross-sectional area of the particles, the larger grain size ensures improved bulk conductivity. Additionally, the vertically oriented porous morphology shortens the average travel distance for charge carriers before they participate in generating photocurrent. The optimal film thickness is limited by the charge carrier diffusion length.

3.5. Scanning electron microscopy (SEM)

SEM analysis (Fig. 5) reveals that the surface morphology of $BiVO_4$ strongly depends on the heating rate, evolving from compact grains at low rates (BV-10 °C) to a porous, cone-like network at BV-60 °C, before collapsing into overgrown coarse features at higher rates (BV-70 °C).

This hierarchical and porous microstructure at BV-60 °C provides an enlarged surface area and facilitates electrolyte infiltration, consistent with AFM measurements that showed the highest surface roughness and nanocone formation for the same sample. XPS analysis further supports this correlation, as BV-60 °C exhibited the most pronounced oxygen-vacancy-related O 1s shoulder and V^{4+} contribution, indicating that the optimized morphology not only promotes surface contact but also provides a favourable environment for defect generation. Quantitative analysis of SEM images revealed average

Table 1 The average arithmetic roughness of the surface (R_a), root mean square vales of the roughness (R_q), and average maximum height (R_{mp}) of as prepared $BiVO_4$ thin films obtained from atomic force microscopy

	Samples names						
Roughness parameter	BV-10 °C	BV-20 °C	BV-30 °C	BV-40 °C	BV-50 °C	BV-60 °C	BV-70 °C
R_a (nm)	15.8	15.7	17.6	21.6	17.7	29.0	20.2
R_q (nm)	19.9	19.6	22.1	27.7	22.7	37.3	25.7
Avg max height (nm)	9.21	7.45	11.4	14.3	13.4	24.0	9.2

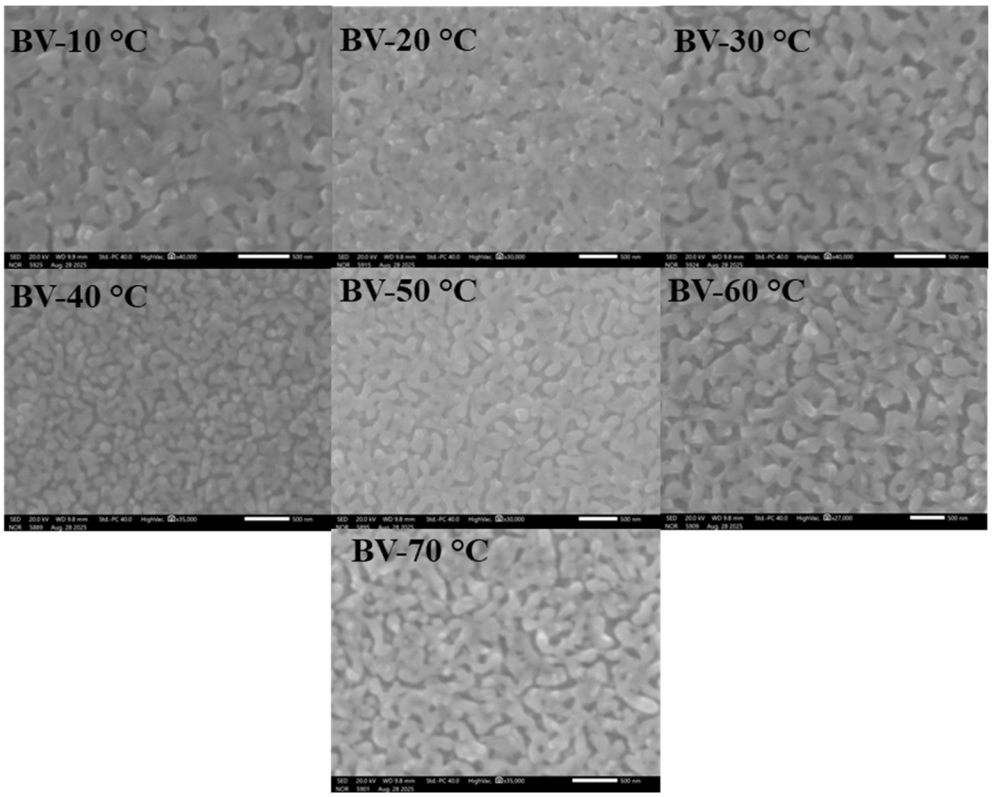

Fig. 5 SEM images of $BiVO_4$ thin films annealed at different heating rates, showing a transition from compact grains (BV-10 °C) to porous, cone-like features at BV-60 °C, followed by overgrown structures at BV-70 °C. The porous nanocone morphology of BV-60 °C provides higher surface area and correlates with AFM roughness and XPS evidence of oxygen vacancies, supporting its improved PEC performance.

grain sizes of ~295 nm, 295 nm, 275 nm, 245 nm, 282 nm, 339 nm, and 280 nm for BV-10 °C to BV-70 °C, respectively, with BV-60 °C exhibiting the largest features. This trend supports the morphological transition observed, where optimized nanocone growth at BV-60 °C provides enhanced porosity and surface area, consistent with AFM roughness and XPS vacancy signatures. Together, these results demonstrate that controlled thermal nucleation simultaneously tunes surface architecture and defect chemistry, leading to improved PEC activity.

3.6. PEC performance

3.6.1. *I–t* curves. The impact of the heating rate on the PEC water splitting performance of $BiVO_4$ films was evaluated using *I–t* curves (Fig. 6a) and *J–V* curves (Fig. 6b) with a conventional three-electrode cell system at a scan rate of 10 mV s^{-1} under AM 1.5 G illumination (100 mW cm^{-2}). Fig. 6a shows the chopped transient current density under SE (substrate to electrolyte) illumination at 1.23 V *vs.* RHE for water splitting. The EE illumination output current density is provided in the SI (Figure S4) and is comparatively lower for all samples due to the increased charge transfer distance for photoelectrons in this configuration. Upon irradiation, the electrodes exhibit a large photocurrent spike due to the presence of numerous photogenerated electron–hole pairs in the bulk. This spike decreases as fast charge carrier recombination balances the charge generation rate. The minimal dark current for all $BiVO_4$ films compared to their photocurrents indicates efficient photoresponse. BV-60 °C demonstrated a remarkable five-fold increase in photocurrent density, reaching 3.17 mA cm^{-2} at 1.23 V *vs.* RHE compared to the initial sample (BV-10 °C). The improved PEC performance is attributed to the morphology defects of the deposited photoanodes, as confirmed by AFM and XPS analyses.

Furthermore, photoluminescence (PL) spectroscopy (Fig. S5, SI note 1) confirmed increased charge carrier mobility and reduced recombination due to the optimized nucleation process through controlled heating rate protocols. The 4.5-hours stability test (Fig. 7) revealed outstanding durability for BV-60 °C in aqueous electrolyte, with only a modest 2% drop in photocurrent density. While BV-10 °C lost 50% of its initial photocurrent density within one hour stability testing. The AFM micrographs justified this expectation, and a detailed discussion on this phenomenon is furnished in the next portion. These results tell that the PEC performance of $BiVO_4$ can be better tuned by optimizing the heating rate during the annealing process of thin films. This strategy predominantly accelerated electron transport and boosted film conductivity. The larger slope of the linear sweep voltammetry (LSV) curves of BV-60 °C substantiates this increase in performance so well as shown in Fig. 6b. To confirm that the enhanced photocurrents were not an artifact of sulfite oxidation, additional PEC measurements were performed in neutral phosphate buffer (KPi, pH 7.0) without a sacrificial agent. As shown in Fig. S8, the

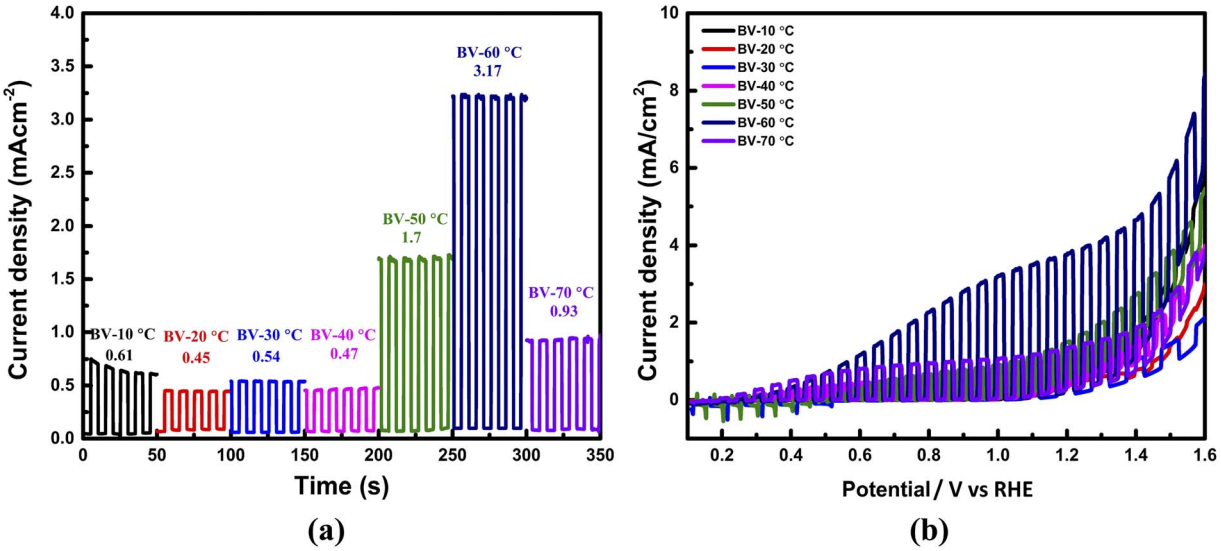

Fig. 6 (a) Chopped transient photocurrent responses of $BiVO_4$ thin films (BV-10 °C to BV-70 °C) measured under SE (substrate-to-electrolyte) illumination at 1.23 V *vs.* RHE, showing variation in current density with heating rate (highest for BV-60 °C at 3.17 mA cm^{-2}). (b) Linear sweep voltammetry (*J*–*V*) curves of the samples, where differences in onset potential and photocurrent trends reflect the influence of heating rate on charge separation and PEC activity.

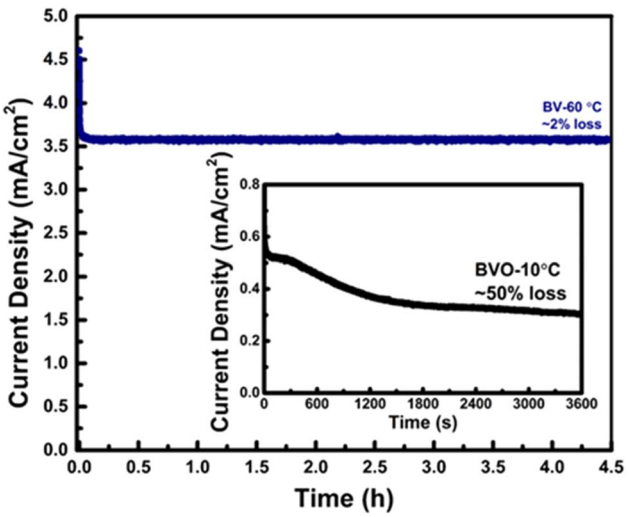

Fig. 7 Stability test of BV-60 °C at 1.23 V *vs.* RHE under continuous illumination for 4.5 h, showing ~2% photocurrent loss. The inset compares BV-10 °C, which exhibits ~50% photocurrent loss within 1 h.

same activity trend was maintained, validating that the improvements arise from intrinsic film properties.

3.6.2. Mott–Schottky plots. Mott–Schottky (MS) measurements were performed to determine the charge carrier density at the $BiVO_4$ electrode–electrolyte interface. The MS curves (Fig. 8a) were obtained from the space charge capacitance values recorded under dark conditions at 1000 Hz. The positive slopes of all curves confirm that $BiVO_4$ is an n-type semiconductor.[76] The slopes indicate that BV-60 °C has a higher charge carrier density compared to other samples. A positive shift in the flat band potential (E_{fb}) for BV-60 °C suggests increased band edge bending, which improves charge separation and aligns with other studies. The Mott–Schottky analysis assumes an ideal depletion region and perfectly ohmic contact between the semiconductor and the electrolyte. While metal oxide semiconductors like $BiVO_4$ may deviate from these assumptions due to interface states or contact resistances, the extracted donor densities here serve as relative indicators because all films share the same thickness, substrate, and electrochemical configuration.[77] Trends from the Mott–Schottky slopes are corroborated by complementary measurements: the systematic increase of V^{4+} ions and oxygen vacancies in XPS, the narrowing of the optical bandgap in UV-vis spectra, suppressed radiative recombination in PL, and reduced charge-transfer resistance in impedance spectra. Collectively, these results confirm that the BV-60 °C sample exhibits the highest effective carrier density, validating the reliability of the comparative analysis.

3.6.3. Electrochemical impedance spectroscopy (EIS). Electrochemical impedance spectroscopy was conducted to characterize the charge mobility at the $BiVO_4$ electrode electrolyte interface. In the Nyquist plots (Fig. 8b), the smaller the diameter of the semicircle, the better the charge carrier transport.[78] The sequence of decreasing semicircle diameters under dark conditions and illumination is BV-20 °C > BV-10 °C > BV-70 °C > BV-40 °C > BV-30 °C > BV-50 °C > BV-60 °C, indicating a significant decrease in charge carrier transfer resistance. The BV-60 °C photoanode effectively suppressed electron–hole pair recombination and exhibited efficient charge mobility, while the BV-70 °C photoanode showed a larger R_{ct} value than BV-30 °C, BV-40 °C, and BV-50 °C, resulting in higher charge transfer resistance. Overly rapid heating rates during annealing led to poor charge transfer at the electrode–electrolyte interface.

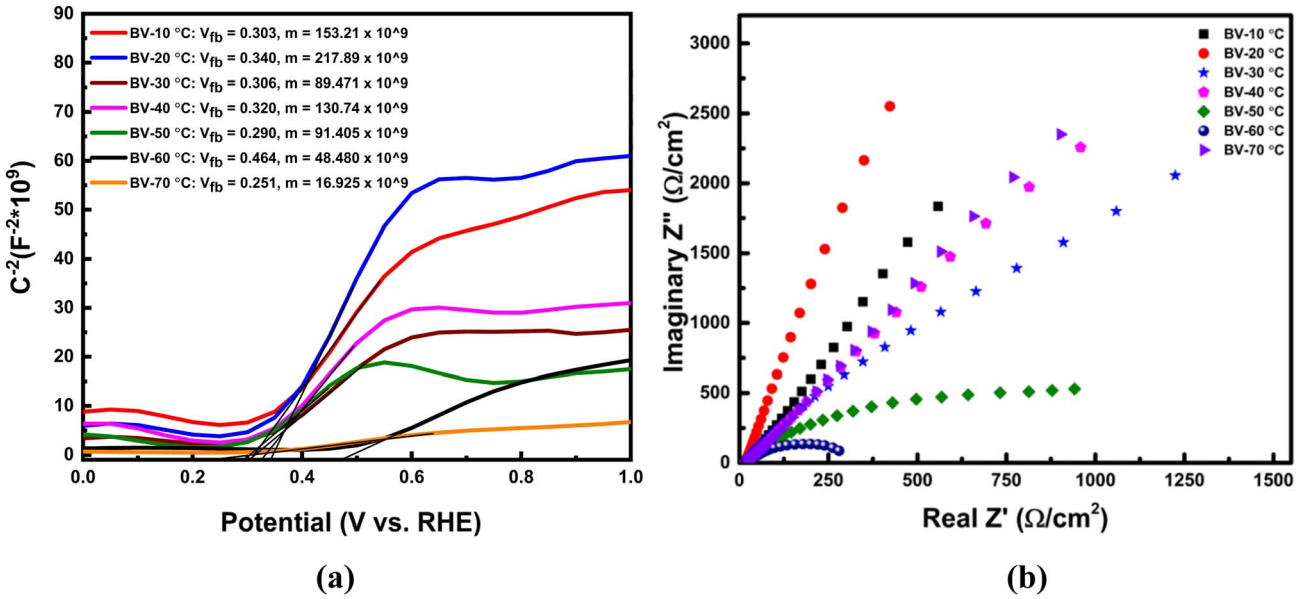

Fig. 8 (a) Mott–Schottky plots of $BiVO_4$ thin films prepared at different heating rates, measured in 0.1 M Na_2SO_4 + 0.1 M Na_2SO_3 electrolyte (pH ~9.26) with 5 mV AC amplitude at 1 kHz. The extracted flat-band potentials (V_{fb}) and slopes (m) are indicated for each sample, showing clear variation with heating rate, and (b) Nyquist plots of $BiVO_4$ thin films under substrate-to-electrolyte illumination, showing differences in charge-transfer resistance (R_{ct}). BV-60 °C displays the smallest semicircle, consistent with faster interfacial charge transfer.

The onset potential of a photoanode is a critical parameter as it reflects the ease of initiating photoelectrochemical water oxidation and can be correlated with the flat band potential obtained from Mott–Schottky analysis. From the LSV curves, the onset potential of BV-60 °C and BV-70 °C is shifted towards more negative values compared to the other samples, indicating that these films require lower external bias to drive charge separation. This trend agrees well with the Mott–Schottky slopes, where BV-60 °C and BV-70 °C exhibit the lowest slopes and therefore the highest donor densities. The higher carrier density facilitates band bending and accelerates charge separation at the semiconductor/electrolyte interface, thereby lowering the onset potential. In contrast, BV-10 °C and BV-20 °C display the highest slopes, corresponding to the lowest donor densities and consequently a delayed onset potential. Although BV-70 °C shows the highest donor density and earliest onset potential, its photocurrent remains lower than BV-60 due to excessive defect states and higher interfacial resistance that promote charge recombination. Hence, BV-60 °C achieves the optimal balance between an advantageous onset potential and suppressed recombination, pronouncing its superior PEC performance. The proposed band alignment and defect-state positions (Fig. 9) are deduced from experimental observations (XPS, UV-vis, PL, and Mott–Schottky analyses).

3.6.4. Incident photon-to-current efficiency (IPCE). The IPCE spectra of the $BiVO_4$ thin films (Fig. 10) were measured at 1.23 V *vs.* RHE under AM 1.5 G illumination in neutral phosphate buffer. BV-60 °C displays the highest IPCE, reaching ~35% at ~420 nm, nearly twice that of BV-20 °C, which shows the weakest response. The relative IPCE intensities mirror the photocurrent trends obtained from LSV, indicating that the enhanced performance of BV-60 °C originates from improved

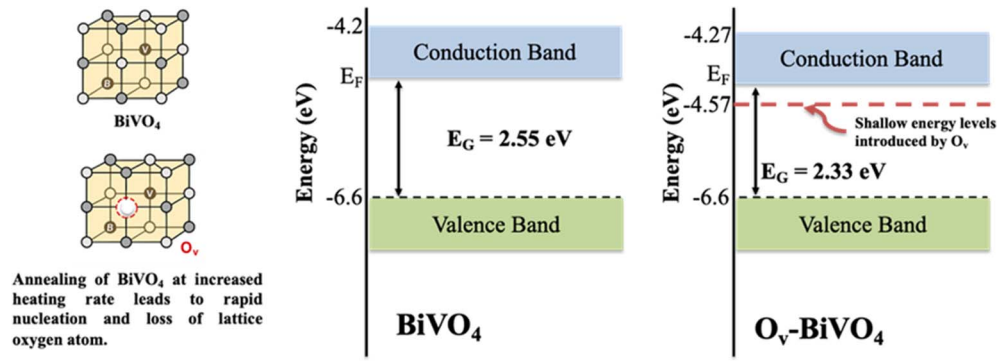

Fig. 9 Rapid Nucleation-induced oxygen vacancy formation in $BiVO_4$: bandgap narrowing and suppressed recombination *via* shallow donor states; an illustration deduced from XPS, UV-vis, PL, and Mott–Schottky analyses.

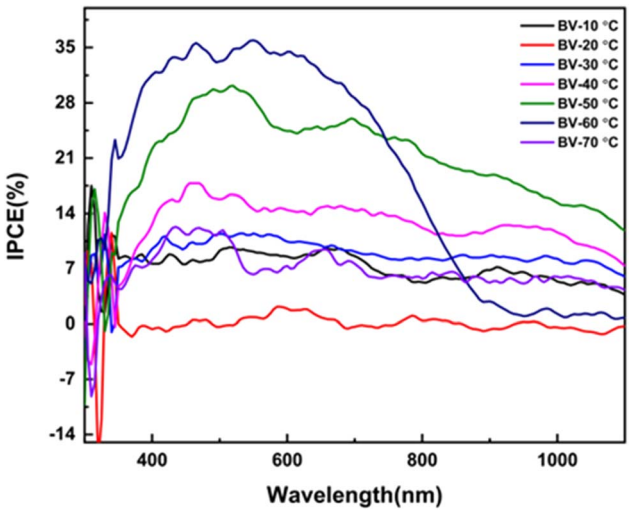

Fig. 10 IPCE spectra of $BiVO_4$ thin films (BV-10 °C to BV-70 °C) showing the highest efficiency for BV-60 °C, consistent with its superior charge separation and PEC performance.

charge separation and reduced recombination associated with oxygen-vacancy-mediated defect states. As the electrolyte does not contain sacrificial agents, the IPCE values directly reflect the intrinsic water oxidation efficiency of the $BiVO_4$ electrodes, confirming that defect engineering *via* controlled thermal nucleation is an effective strategy for boosting photoanode performance.

3.7. Theoretical insights into oxygen vacancy-mediated electronic modulation in $BiVO_4$

To investigate the electronic origins of the enhanced photoactivity, DFT calculations were performed on pristine and oxygen deficient $BiVO_4$ supercells. Fig. 11a and b show the calculated band structures. The pristine system exhibits a direct bandgap of 2.6 eV, consistent with our experimental optical gap of 2.55 eV. Upon introduction of an oxygen vacancy, a defect band appears that reduces the calculated gap to 2.2 eV, corresponding to the redshift observed experimentally for BV-60 °C. The projected density of states (PDOS) for the pristine and oxygen deficient systems are shown in Fig. 11c and d, respectively. In the oxygen deficient system, a new peak composed of V 3d orbitals emerges approximately 0.4 eV below the conduction band minimum, representing V^{4+} derived shallow donor states.[79] This feature is consistent with the V^{4+} species identified in our XPS analysis.

These vacancy-induced states enable lower energy electronic transitions,[79] accounting for the enhanced visible light absorption in BV-60 °C. Previous computational work has shown that concurrent optimization of band structure and oxygen vacancy concentration is critical for maximizing photoelectrochemical performance.[80] The calculated band structures (Fig. 11a and b) also reveal modified conduction band dispersion in the defective system, indicating improved electron transport. This finding aligns with the increased carrier density extracted from our Mott Schottky analysis and the reduced charge transfer resistance observed in EIS for BV-60 °C.

Work functions were calculated from planar averaged electrostatic potential profiles (Fig. 11e and f). The pristine slab yields a work function of 5.64 eV, while the oxygen deficient slab exhibits a reduced value of 5.32 eV ($\Delta\Phi$ = 0.32 eV). This reduction results from the upward shift of the Fermi energy into oxygen vacancy donor states, consistent with the enhanced n type character observed in our Mott Schottky analysis.

Beyond band structure modification, the asymmetric charge distribution induced by oxygen vacancies disrupts the local symmetry of the $BiVO_4$ lattice, generating a local dipole moment.[81] This dipole creates an internal electric field that promotes electron hole separation, consistent with the quenched photoluminescence observed in BV-60 °C (Fig. S5). Collectively, these DFT calculations confirm that oxygen vacancies introduce shallow donor states that narrow the bandgap, increase carrier density, lower the work function, and enhance charge separation, contributing to the superior PEC performance of BV 60 °C.

3.8. Mechanism of defect-mediated charge transport mechanism in $BiVO_4$ photoanodes induced by controlled thermal nucleation

During annealing procedure, the formation of O_v takes place in $BiVO_4$ lattice through a controlled heating rate protocol that encourage slight lattice oxygen loss and the concomitant partial reduction of V^{5+} to V^{4+}. These oxygen vacancies act as shallow donor sites, introducing electronic states just below the conduction band (as depicted in the Fig. 9). These O_v-related defect levels lie right under the conduction band edge, which effectively dopes the $BiVO_4$ lattice with n-type defects. Density functional theory calculations corroborate this mechanism by revealing V^{4+}-derived shallow donor states located near the conduction band minimum, which induce bandgap narrowing and an upward Fermi-level shift. The presence of these donor levels narrows the effective band gap from ~2.55 eV in pristine $BiVO_4$ to ~2.33 eV in O_v-rich $BiVO_4$ by enabling lower-energy electronic transitions. As a result of this reduction in band gap, visible light is absorbed into longer wavelengths, resulting in better photon utilization. Moreover, oxygen vacancies increase the electron carrier density (since each O_v donates two electrons), which improves electrical conductivity and facilitates charge separation. The shallow donor states trap photogenerated electrons away from the valence band, lowering the likelihood of electron–hole recombination and thus suppressing radiative recombination pathways.

Experimentally, X-ray photoelectron spectroscopy (XPS) provides evidence of this mechanism: O_v-rich $BiVO_4$ exhibits a shoulder in the O 1s XPS peak (around ~531.5 eV) and an increased V^{4+} signal, directly indicating oxygen vacancies and the reduction of V^{5+} to V^{4+}. In O_v-modified $BiVO_4$, the absorption edge marks a significant redshift, consistent with a narrower band gap. Likewise, photoluminescence (PL) measurements reveal a quenched emission intensity for O_v-engineered $BiVO_4$, signifying reduced charge-carrier recombination. These experimental observations are in agreement with the theoretical predictions of defect-induced donor levels and

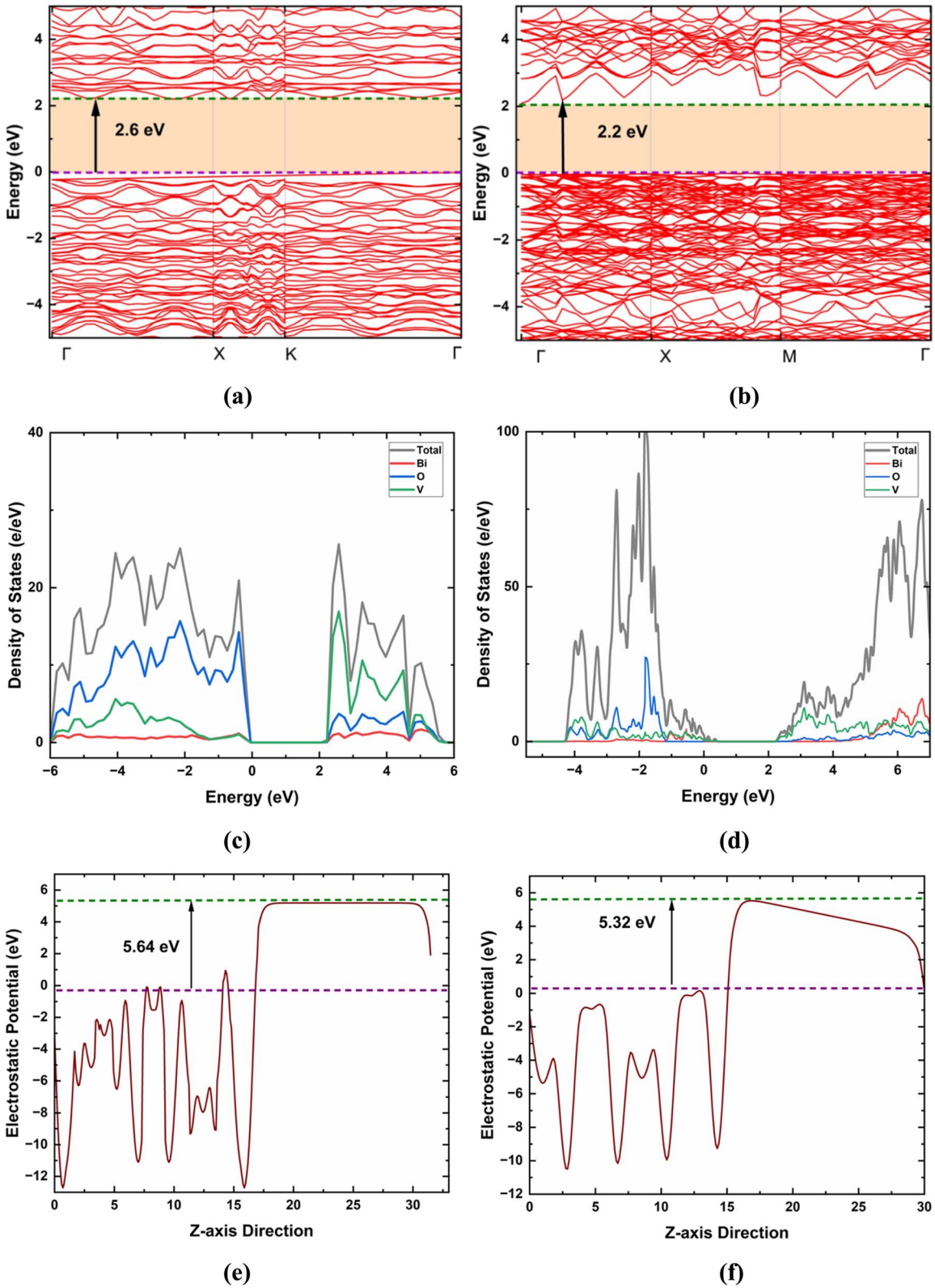

Fig. 11 (a and b) Electronic band structures of pristine and oxygen-deficient $BiVO_4$, showing bandgap narrowing from 2.6 to 2.2 eV due to vacancy-induced defect states. (c and d) Total and projected density of states (PDOS) illustrating atomic contributions and the emergence of V-derived donor states in oxygen-deficient $BiVO_4$. (e and f) Planar-averaged electrostatic potential profiles used for work-function calculations, yielding $\Phi = 5.64$ eV (primitive) and 5.32 eV (defective).

enhanced n-type character, establishing a direct correlation between electronic-structure modulation and photoelectrochemical performance. The synergic effects of reduced band gap increased visible-light absorption, and improved charge separation with lower recombination align with the depiction of pristine *versus* O_v-modified $BiVO_4$ in the Fig. 8. The O_v-rich $BiVO_4$ features defect-derived donor levels below the conduction band that boost its photoactivity, whereas the pristine $BiVO_4$ retains a wider band gap and suffers from more recombination, underscoring the beneficial role of oxygen vacancy engineering in $BiVO_4$.

4 Conclusion

$BiVO_4$ films were deposited by spin coating and annealed at 475 °C with varying heating rates to tune nucleation process. XRD analysis revealed that all samples exhibited a monoclinic scheelite structure. The porosity in the morphology of BV-60 °C increased the effective surface area and improved electrolyte contact, facilitating interfacial charge transfer. This sample also possessed a high concentration of oxygen vacancies and V^{4+} ions in its lattice, which enhanced photon absorption, charge generation, and charge mobility. These morphological and electronic defects reduced the bandgap energy from 2.55 eV to 2.33 eV and resulted in a five-fold increase in photocurrent density to 3.17 mA cm^{-2} for pristine $BiVO_4$.

DFT calculations further demonstrated that these oxygen vacancies introduce V^{4+}-derived shallow donor states, which contribute to bandgap narrowing and modify conduction band dispersion to facilitate charge transport. At an annealing rate of 60 °C min^{-1}, the concentration of oxygen vacancies appears sufficient to balance improved carrier mobility with reduced recombination losses without introducing excessive structural defects that may act as recombination centres, as observed at higher ramping rates (*e.g.*, 70 °C min^{-1}). Thus, the optimized defect chemistry induced by thermal treatment tailors the band structure to improve light harvesting, charge separation, and interfacial charge transfer, collectively enhancing PEC water splitting performance.

The 4.5-hours stability test demonstrated that tuning the thermal conditions during $BiVO_4$ thin film deposition produces an efficiently photoactive material capable of withstanding aqueous electrolyte for extended periods, preventing short circuiting. This synthesis approach may also be extended to explore the defect-mediated intrinsic properties of other functional metal oxides, advancing their potential for photocatalytic applications.

Author contributions

Rafiqat Ul Rasool: conceptualization, methodology, investigation, data curation, formal analysis, visualization, writing-original draft, review & editing. Syed Bilal Ahmed: formal analysis, theoretical calculations, writing-review & editing. Ruiqin Zhang: supervision, resources, project administration, funding acquisition, writing-review & editing.

Conflicts of interest

There are no conflicts to declare.

Data availability

All data supporting the findings of this study are available within the article and its supplementary information (SI) file. The data will be available from the corresponding author upon reasonable request. Supplementary information: comparative analysis of reported $BiVO_4$ systems, additional experimental details, structural and spectroscopic characterization, and supporting photoelectrochemical performance data of $BiVO_4$ thin films. See DOI: https://doi.org/10.1039/d5ta03464g.

Acknowledgements

This work was supported by the Research Grants Council of the Hong Kong SAR (No. 11317122) and the City University of Hong Kong (No. 9231264, 7020044, 9229019, 7020096).

References

1 H. Wu, L. Zhang, A. Du, R. Irani, R. van de Krol, F. F. Abdi and Y. H. Ng, *Nat. Commun.*, 2022, **13**, 6231.
2 A. Vilanova, P. Dias, T. Lopes and A. Mendes, *Chem. Soc. Rev.*, 2024, **53**, 2388–2434.
3 D. J. Martin, P. J. T. Reardon, S. J. A. Moniz and J. Tang, *J. Am. Chem. Soc.*, 2014, **136**, 12568–12571.
4 S. Wei, X. Xia, S. Bi, S. Hu, X. Wu, H.-Y. Hsu, X. Zou, K. Huang, D. W. Zhang, Q. Sun, A. J. Bard, E. T. Yu and L. Ji, *Chem. Soc. Rev.*, 2024, **53**, 6860–6916.
5 M. G. Walter, E. L. Warren, J. R. McKone, S. W. Boettcher, Q. Mi, E. A. Santori and N. S. Lewis, *Chem. Rev.*, 2010, **110**, 6446–6473.
6 A. Currao, *Chimia*, 2007, **61**, 815–819.
7 A. Fujishima and K. Honda, *Nature*, 1972, **238**, 37–38.
8 S.-C. Wang, F.-Q. Tang and L.-Z. Wang, *J. Inorg. Mater.*, 2018, **33**, 173–197, DOI: 10.15541/jim20170352.
9 N. Serpone and A. Emeline, *J. Phys. Chem. Lett.*, 2012, **3**, 673–677.
10 J. Wang, M. Zhou, H. Yu, Z. Zhang and Y. Sun, *J. Colloid Interface Sci.*, 2025, **646**, 35–46.
11 S. Hwang, M. Yang, C. Kim, J. Lee and J. Kim, *Sustain. Energy Fuels*, 2020, **4**, 1437–1442.
12 J. D. Butson, J. Tournet, B. Gupta, A. Sharma, M. Lysevych, T. Haggren, C. Jagadish, H. H. Tan and S. Karuturi, *ACS Appl. Mater. Interfaces*, 2024, **16**, 45180–45188.
13 Y. Ramprakash, D. Bose and S. Basu, *Surf. Sci.*, 1984, **145**, 175–184.
14 K.-S. Ahn, Y. Yan, S. H. Wei and J. A. Turner, *Appl. Phys. Lett.*, 2008, **93**, 163117.
15 H. S. Mansur, M. A. Orefice and A. C. Mansur, *J. Chem. Soc., Faraday Trans.*, 1995, **91**, 665–672, DOI: 10.1039/FT9959100665.
16 J. Zhang, X. Wu, Y. Liu, H. Chen and S. Li, *J. Mater. Chem. A*, 2015, **3**, 535–541.

17 S. Chen, T. Takata and K. Domen, *Nat. Rev. Mater.*, 2017, **2**, 17050.
18 J. Jia, M. Seitz, J. Lichterman, N. Liu and H. Wang, *Nat. Commun.*, 2016, **7**, 1–6.
19 P. Guo, F. Hao, L. Chen, W. Hu and Y. Fang, *J. Mater. Chem. A*, 2019, **7**, 2497–2506.
20 J. H. Kim, D. H. Youn, J. Y. Kim, S. K. Lim and J. S. Lee, *Nat. Commun.*, 2016, **7**, 1–9.
21 X. Shi, H. Wang, C. Chen, J. Liu and T. Zhang, *Nat. Commun.*, 2016, **7**, 1–6.
22 B. Y. Liu, J. Wang, X. Lin, Y. Zhao and H. Zhang, *Angew. Chem., Int. Ed.*, 2023, **62**, e202217346.
23 F. Wang, M. Li, Y. Xu, S. Tang and X. Wang, *J. Am. Chem. Soc.*, 2017, **139**, 15094–15103.
24 A. Walsh, J. L. F. Da Silva and S. H. Wei, *Chem. Mater.*, 2009, **21**, 547–551.
25 K. Sivula, F. Le Formal and M. Grätzel, *ChemSusChem*, 2011, **4**, 432–449.
26 F. F. Abdi, L. Han, A. H. M. Smets, M. Zeman, B. Dam and R. van de Krol, *J. Phys. Chem. Lett.*, 2013, **4**, 2752–2757.
27 A. Bhattacharya, K. Mallick and A. Hartridge, *Mater. Lett.*, 1997, **30**, 7–13.
28 Y. Zhao, C. Zhang, H. Xu, L. Wang and G. Chen, *Chem.–Eur. J.*, 2008, **14**, 1601–1606.
29 J. K. Cooper, S. Gul, F. M. Toma, I. D. Sharp, L. Y. Lin and J. W. Ager, *J. Phys. Chem. C*, 2015, **119**, 2969–2974.
30 F. Ye, M. Chen, J. Zhang, L. Wei and S. Huang, *Appl. Catal., B*, 2018, **227**, 258–265.
31 H. S. Han, S. Shin, D. Jeong, Y. J. Jang and J. S. Lee, *Energy Environ. Sci.*, 2018, **11**, 1299–1306.
32 F. F. Abdi, L. Han, A. H. M. Smets, M. Zeman, B. Dam and R. van de Krol, *Nat. Commun.*, 2013, **4**, 1–7.
33 K. P. S. Parmar, H. J. Kang, J. S. Lee and J. H. Kim, *ChemSusChem*, 2012, **5**, 1926–1934.
34 J.-S. Yang and J.-J. Wu, *Nano Energy*, 2017, **32**, 232–240.
35 L. Zhou, M. Xu, C. Wang, W. Li and X. Zhang, *Nano Lett.*, 2016, **16**, 3463–3474.
36 L. Zhang, L. O. Herrmann and J. J. Baumberg, *Sci. Rep.*, 2015, **5**, 1–12.
37 W. Yang, Q. Li, Z. Li, T. Wang and X. Wang, *Nanoscale Res. Lett.*, 2016, **11**, 1–8.
38 Y. Wei, Y. Zhang, X. Liu and H. Li, *Nano Res.*, 2016, **9**, 1561–1569.
39 J. S. Nyarige, T. P. Krüger and M. Diale, *Mater. Today Commun.*, 2020, **25**, 101459.
40 H. Baqiah, M. Ali, N. Z. Noor and A. Salleh, *Optik*, 2020, **206**, 164303.
41 S. Zhang, J. Wang, M. Li, Y. Chen and X. Liu, *Appl. Catal., B*, 2020, **262**, 118279.
42 Z. Masoumi, M. Tayebi and B.-K. Lee, *Ultrason. Sonochem.*, 2021, **72**, 105403.
43 B. Wickman, A. Bastos da Silva Fanta, A. Burrows, A. Hellman, J. B. Wagner and B. Iandolo, *Sci. Rep.*, 2017, **7**, 40500.
44 L. Shi, S. Zhuo, M. Abulikemu, G. Mettela, T. Palaniselvam, S. Rasul, B. Tang, B. Yan, N. B. Saleh and P. Wang, *RSC Adv.*, 2018, **8**, 29179–29188, DOI: 10.1039/C8RA04887H.
45 V. D. Das, J. Sathyanarayanan and L. Damodare, *Surf. Coat. Technol.*, 1997, **94**, 669–671.
46 F. F. Abdi and R. van de Krol, *J. Phys. Chem. C*, 2012, **116**, 9398–9404.
47 H. Fu, Q. Qi, Y. Li, J. Pan and C. Zhong, *Nanomaterials*, 2024, **14**, 1270.
48 B. D. Khadka, S. Sagadevan, S. Kato and T. Soga, *Phys. B: Condens. Matter*, 2024, **682**, 415878.
49 R. Chen, M. Li, S. Hu and J. Wang, *ChemElectroChem*, 2024, **11**, e202400600.
50 G. C. Tu, J. Y. Chen, Y. Li, C. W. Chang, W. J. Chang, Z. X. Zhen, H. M. Chen and C. M. Jiang, *ACS Appl. Electron. Mater.*, 2024, **6**, 1872–1885.
51 A. Choi, M. Jung and Y. K. Lee, *Electrochem. Solid-State Lett.*, 2009, **12**, 7–10.
52 J. R. Frade, *J. Am. Ceram. Soc.*, 2005, **81**, 2654–2660.
53 M. Lamers, S. Fiechter, D. Friedrich, F. F. Abdi and R. van de Krol, *J. Mater. Chem. A*, 2018, **6**, 18694–18700, DOI: 10.1039/C8TA06269B.
54 Q. Zhang, S. Jiang and Y. Li, *Surf. Rev. Lett.*, 2007, **14**, 141–145.
55 G. Kresse and J. Hafner, *Phys. Rev. B: Condens. Matter Mater. Phys.*, 1993, **47**, 558.
56 G. Kresse and J. Hafner, *Phys. Rev. B: Condens. Matter Mater. Phys.*, 1994, **49**, 14251.
57 J. P. Perdew, K. Burke and M. Ernzerhof, *Phys. Rev. Lett.*, 1996, **77**, 3865.
58 P. E. Blöchl, *Phys. Rev. B: Condens. Matter Mater. Phys.*, 1994, **50**, 17953.
59 H. J. Monkhorst and J. D. Pack, *Phys. Rev. B: Condens. Matter Mater. Phys.*, 1976, **13**, 5188.
60 S. A. A. Terohid, S. Heidari, A. Jafari and S. Asgary, *Appl. Phys. A*, 2018, **124**, 1–9.
61 D. Jena and A. Konar, *Phys. Rev. Lett.*, 2007, **98**, 136805.
62 Y. S. Son, Y. Kim, J. Lee, G. Y. Lee, W. T. Park, Y. Y. Noh, C. E. Park and T. Park, *J. Am. Chem. Soc.*, 2016, **138**, 8096–8103.
63 K. Zhang, L. Wang, T. Liu and X. Li, *Nat. Commun.*, 2019, **10**, 1–10.
64 W. Luo, M. Li, Q. Chen and R. Zhang, *Energy Environ. Sci.*, 2011, **4**, 4046–4051.
65 L. Zhang, D. Chen and X. Jiao, *J. Phys. Chem. B*, 2006, **110**, 2668–2673.
66 M. F. R. Samsudin, R. Bashiri, N. M. Mohamed, Y. H. Ng and S. Sufian, *Appl. Surf. Sci.*, 2020, **504**, 144417.
67 F. S. Hegner, D. Forrer, J. R. Galán-Mascarós, N. López and A. Selloni, *J. Phys. Chem. Lett.*, 2019, **10**, 6672–6678, DOI: 10.1021/acs.jpclett.9b02552.
68 M. Huang, J. Bian, W. Xiong, C. Huang and R. Zhang, *J. Mater. Chem. A*, 2018, **6**, 3602–3609, DOI: 10.1039/C7TA11132K.
69 F. Li, H. Wu, Z. Liu and Y. Yang, *Phys. Chem. Chem. Phys.*, 2017, **19**, 21862–21868.
70 G. Tan, Y. Zhang, L. Zhang and Z. Zhang, *Ceram. Int.*, 2014, **40**, 9541–9547.
71 M. Wang, Q. Li, J. Zhou and L. Zhang, *J. Alloys Compd.*, 2015, **648**, 1109–1115.

72 C. Q. Sun, *Prog. Solid State Chem.*, 2006, **35**, 1–159.
73 Z. Zhao, X. Li, H. Liu and Y. Wang, *Solid State Sci.*, 2013, **18**, 98–104.
74 J. Yu and A. Kudo, *Chem. Lett.*, 2005, **34**, 850–851.
75 J.-M. Wu, Y.-H. Lin and H.-S. Tsai, *Appl. Catal., B*, 2018, **221**, 187–195.
76 A. Hankin, M. Bedoya-Lora, J. C. Alexander, A. Regoutz and G. H. Kelsall, *J. Mater. Chem. A*, 2019, **7**, 26162–26176.
77 A. Venugopal, R. Kas, K. Hau and W. A. Smith, *J. Am. Chem. Soc.*, 2021, **143**, 18581–18591, DOI: 10.1021/jacs.1c08245.
78 Y. Bicer and I. Dincer, *Chem. Eng. Process. Process Intensif*, 2017, **117**, 141–153, DOI: 10.1016/j.cep.2017.04.001.
79 O. El Ouardi, H. Ladib, B. Vigolo, J. Alami and M. Makha, *Int. J. Hydrogen Energy*, 2025, **157**, 150384, DOI: 10.1016/j.ijhydene.2025.150384.
80 P. An, Y. Zhou, H. Xiu, Y. Wang and Y. Wang, *J. Colloid Interface Sci.*, 2026, 140231.
81 J. Zhang, Q. Jia and M. Li, *Dalton Trans.*, 2026, **55**, 3, DOI: 10.1039/D5DT02584B.